UAB
Universitat Autònoma de Barcelona

UNIVERSITAT AUTÒNOMA DE BARCELONA
FACULTAT DE CIÈNCIES
DEPARTAMENT DE FÍSICA

TREBALL FINAL DE GRAU EN FÍSICA

CHARACTERIZATION OF THE BARCELONA RAMAN LIDAR

ALBA APIO SANTOS

SUPERVISOR:
DR. MARKUS GAUG

Abstract

This thesis presents an optical characterization of key components of the Barcelona Raman Lidar system, focusing on a newly integrated laser and the Newtonian reflector. The aim was to evaluate their current performance and identify optical limitations that may impact the quality of atmospheric measurements. The laser beam was analysed by comparing experimental irradiance profiles with theoretical models. A circular Hermite-Gaussian model was found to be insufficient to describe the observed beam shape, while an elliptical Gaussian model offered a significantly better fit. The retrieved beam quality factor was $M^2 = 1.42 \pm 0.17$, although a reduced chi-squared value of $\chi^2/\mathrm{ndf} = 2.02$ suggests remaining discrepancies between model and data that require further study. The mirror's optical response was evaluated by measuring its point spread function. Compared to the original characterization, the current mirror shows strong aberrations, making it unsuitable for further use. A replacement mirror was installed, but its performance could not be tested within the scope of this project. All in all, this work highlights the importance of accurate optical diagnostics for improving the Raman Lidar's performance and offers valuable insights for future system optimization.

Jo, **Alba Apio Santos**, amb Document Nacional de Identitat **47574630G**, i estudiant del Grau en Física de la Universitat Autònoma de Barcelona, en relació amb la memòria del treball de final de Grau presentada per a la seva defensa i avaluació durant la convocatòria de Juliol del curs 2024-25, declara que:

- El document presentat és original i ha estat realitzat per la seva persona.

- El treball s'ha dut a terme principalment amb l'objectiu d'avaluar l'assignatura de treball de grau en física en la UAB, i no s'ha presentat prèviament per ser qualificat en l'avaluació de cap altre assignatura ni aquesta ni en cap altre universitat.

- En el cas de continguts de treballs publicats per terceres persones, l'autoria està clarament atribuïda, citant les fonts degudament.

- En els casos en els que el meu treball s'ha realitzat en col·laboració amb altres investigador i/o estudiants, es declara amb exactitud quines contribucions es deriven del treball de tercers i quines es deriven de la meva contribució.

- A l'excepció del punts esmentats anteriorment, el treball presentat és de la meva autoria.

Signat:

Declaració d'Extensió del Treball de Grau

Jo, **Alba Apio Santos**, amb Document Nacional de Identitat **47574630G**, i estudiant del Grau en Física de la Universitat Autònoma de Barcelona, en relació amb la memòria del treball de final de Grau presentada per a la seva defensa i avaluació durant la convocatòria de Juliol del curs 2024-2025, declara que:

- El nombre total de paraules (segons comptatge proposat)[1] incloses en les seccions des de la introducció a les conclusions és de **7791** paraules.

- El nombre total de figures és de **8**.

- El nombre total d'equacions i línies de taules és de **30**.

En total, el document comptabilitza:

7791 paraules + **8** x 200 paraules/figura + **30** paraules/equació i taula = **9991** paraules.

Que compleix amb la normativa al ser inferior a 10000.

Signat:

---

[1]Utilitzant l'eina de comptatge de paraules de Word. La versió Word 365, amb llicència de campus UAB, permet obrir arxius pdf. Per tal de fer el comptatge s'ha seleccionat el text des de la introducció fins a les conclusions, excloent equacions i taules. Queden exclosos del comptatge: abstract, referencies, annexos i qualsevol document que no formi part pròpiament del cos del treball

Contents

1   Introduction, objectives and motivation

Understanding the optical behaviour of atmospheric monitoring instruments is essential for improving the research on environmental and astronomical topics. In particular, the Barcelona Raman Lidar (BRL) [1] has been developed as part of the atmospheric calibration strategy of the Cherenkov Telescope Array Observatory (CTAO) [2, 3], the world's next-generation very high-energy gamma-ray observatory. Since CTAO relies on the detection of Cherenkov light produced by particle cascades created by gamma rays interacting with the atmosphere, it is crucial to continuously monitor atmospheric conditions.

In this context, Lidar systems, which allow for remote sensing of the atmosphere through laser-based techniques, help to correct for systematic errors caused by atmospheric variability and to improve the data collected under non-ideal weather conditions. The motivation for this project is the opportunity to deepen knowledge in optics, laser physics and data analysis in a real research environment, and contribute to such efforts by helping to improve the performance of the BRL.

The main objective of this project is to understand the functionality of several key components of the BRL. This work has been carried out under the supervision of the BRL team and combines theoretical study with experimental data analysis.

Specific goals include learning how a Lidar system works, the theoretical description of laser beams and their propagation in the far field, and testing the focal distance of the mirror. The mirror's optical aberrations are characterized and analysed to evaluate their effect on the system's performance. The project also involves improving and applying methods for beam parameter reconstruction from images, as well as processing and interpreting real data collected from the system.

The methodology included a review of relevant literature, measurements of the laser beam and the mirror, and the development of Python scripts for data analysis.

On a personal level, this project aims to consolidate knowledge acquired during the degree, improve skills in experimental methods and programming, and apply the scientific method in a real research context. Although not all objectives may be fully achieved, the overall experience contributes significantly to academic and personal growth.

2 Theoretical background

2.1 Lidar systems

Lidar (Light Detection and Ranging) is an optical remote sensing technique that enables the measurement of atmospheric properties over long distances with high spatial and temporal resolution. It works by sending short pulses of laser light into the atmosphere and detecting the light backscattered by molecules and particles suspended in air. The distance to the scattering point can be accurately determined by measuring the time delay between emission and reception, as the laser pulse travels at the speed of light.

A typical Lidar system consists of a laser that generates coherent and monochromatic light pulses, aligned with the optical axis of a telescope. The telescope, most commonly a curved mirror, collects the backscattered light and focuses it on photodetectors, typically photomultiplier tubes (PMTs). These detectors convert photons into an electronic signal that can be processed and analysed. The system can be configured to detect different types of scattering processes, namely elastic and inelastic scattering. Each type provides different information about atmospheric properties.

Due to its flexibility and sensitivity, Lidar has become one of the most powerful tools for atmospheric remote sensing, as no other technique can measure as many atmospheric parameters with the same level of precision. Different types of Lidar can retrieve vertical profiles of aerosols, clouds, water vapour, or even wind speed through the analysis of the intensity and spectral content of the returned signals [4].

The amount of light backscattered from a given point in the atmosphere depends on two main factors: the attenuation suffered by the laser radiation along its path, and the local backscatter cross-section, which characterizes the scattering efficiency of atmospheric particles and molecules. Molecules scatter light via Rayleigh scattering; their cross-section depends only on the wavelength. In contrast, the aerosol backscatter cross-section is influenced by aerosol composition, size and shape. Therefore, variations in aerosol properties directly affect the strength of the backscattered signal [5].

The relation between transmitted and received powers is described by the Lidar equation:

$$P(r,\lambda) = P_0 \frac{Act_0}{2r^2} \beta(r,\lambda) e^{-2\tau(r,\lambda)} \tag{1}$$

where $P(r,\lambda)$ is the received power from a distance r at wavelength λ, P_0 is the emitted laser power, c the speed of light, t_0 the laser pulse duration, A the effective area of the receiver telescope, $\beta(r,\lambda)$ the backscatter coefficient, and $\tau(r,\lambda)$ the optical depth.

The optical depth represents the cumulative attenuation of the laser signal due to both scattering and absorption along the laser path. It is defined as:

$$\tau(r,\lambda) = \int_0^r \alpha(r',\lambda) dr' \tag{2}$$

where $\alpha(r,\lambda)$ is the extinction coefficient, which quantifies the loss of intensity per unit distance.

Generally, both $\alpha(r,\lambda)$ and $\beta/r,\lambda)$ can be decomposed into contributions from molecular and aerosol components.

$$\alpha(r,\lambda) = \alpha_{\mathrm{mol}}(r,\lambda) + \alpha_{\mathrm{aer}}(r,\lambda) \qquad\qquad \beta(r,\lambda) = \beta_{\mathrm{mol}}(r,\lambda) + \beta_{\mathrm{aer}}(r,\lambda) \tag{3}$$

Similarly, $\alpha(r,\lambda)$ can be separated into scattering and absorption contributions:

$$\alpha(r,\lambda) = \alpha_{\mathrm{scatt}}(r,\lambda) + \alpha_{\mathrm{abs}}(r,\lambda) \tag{4}$$

where α_{scatt} accounts for light scattered out of the beam and α_{abs} for intensity lost by absorption. In practice, molecular absorption is negligible at typical Lidar wavelengths of 355 nm and 532 nm, but becomes significant in the infrared range.

The molecular contributions can be computed from Rayleigh theory, with only one unknown parameter: the number density of air molecules, which need to be assessed with radio-sonde and satellite measurements. Conversely, the aerosol backscatter cross-section is governed by Mie theory or even more complex

scattering models, and depends on the aerosol size distribution, composition, and shape, parameters that are highly variable and generally unknown. Therefore, with a traditional elastic-backscatter Lidar (detecting only backscattered signal at the same wavelength as the emitting laser), Eq. (1) contains two unknowns: $\beta_{\text{aer}}(r, \lambda)$ and $\tau_{\text{aer}}(r, \lambda)$. Both quantities appear combined in the detected signal and cannot be retrieved simultaneously without making additional assumptions. Furthermore, these quantities are functions of distance and wavelength, since different atmospheric constituents and processes interact differently with light at different wavelengths [5].

Different strategies overcome this limitation. One approach assumes a constant or parametrized value of the Lidar Ratio (LR), defined as the ratio of aerosol extinction to aerosol backscatter:

$$\text{LR} = \frac{\alpha_{\text{aer}}(r, \lambda)}{\beta_{\text{aer}}(r, \lambda)} \; , \tag{5}$$

based on climatological data or models.

However, this assumption depends on aerosol type and atmospheric conditions. More robust solutions use advanced Lidar systems such as Raman Lidars, which detect inelastically scattered light from specific molecules, or High Spectral Resolution Lidars (HSRL), which distinguish aerosol and molecular backscatter by using the spectral broadening of the molecular return.

2.2   Scattering in the atmosphere

When a laser pulse travels through the atmosphere, it interacts with molecules and aerosols, leading mainly to scattering and absorption processes. In a scattering process, the incident photon is deflected by a particle. This can occur elastically, with no change in frequency, or inelastically, involving an energy exchange between light and matter, causing a frequency shift of the scattered light. In an absorption process, the photon is absorbed by the molecule, transferring its energy to excite the molecule to a higher internal state.

Scattering is the fundamental mechanism exploited in Lidar systems, as it provides the measurable return signal needed to infer atmospheric properties. The type of scattering directly affects the quality and nature of the data obtained. The main scattering processes relevant in this context are described below [6, 4]:

Rayleigh Scattering
Rayleigh scattering occurs when light interacts with particles much smaller than its wavelength, typically atmospheric molecules. It is an elastic process, meaning the scattered photon retains the same energy and frequency. The Rayleigh scattering cross-section, which quantifies the probability of scattering, scales with λ^{-4}, so shorter wavelengths scatter more efficiently [7, 8]. While Rayleigh scattering is crucial for understanding the general atmospheric structure, it does not provide chemical specificity, making it less useful for identifying atmospheric constituents.

Mie scattering
Mie scattering involves particles comparable to or larger than the wavelength of the incident photon, like aerosols, assumed to be spherical. It is also an elastic process, but with a weaker wavelength dependence. The cross-section approximately follows $\sigma \propto \lambda^{-k}$, where k is the Ångström exponent. This exponent provides insight into the relative size of the scattering: values of $k \approx 4$ indicate small particles (Rayleigh-like-behaviour), while values of $k \approx 0$ imply large particles, with nearly wavelength-independent (grey) scattering. Like Rayleigh scattering, Mie scattering does not provide direct information about particles' chemical composition.

Raman scattering

Raman scattering is an inelastic light-matter interaction that forms the physical basis of Raman Lidar systems. It enables remote sensing of atmospheric composition and is key to independently retrieving the LR. When a monochromatic laser beam of frequency ν interacts with atmospheric molecules, most photons are elastically scattered. However, a small fraction undergoes Raman scattering, emerging with a shifted frequency ν_R due to an energy exchange with the molecule.

Molecules have internal structure, with their electronic ground state split into multiple vibrational and rotational sublevels. In Raman scattering applications of Lidar, the incident photon excites a vibrational mode, and the molecule then relaxes into the vibrational ground state of different rotational levels. This energy exchange leads to a frequency shift in the scattered photon. If the molecule gains energy, the scattered photon has less energy than the incident one, resulting in a Stokes shift process. However, if the molecule loses energy, the photon gains energy, and the process is an Anti-Stokes shift.

In practice, vibrational Raman lines appear as broadened spectral bands due to accompanying rotational transitions. Each vibrational shift includes a distribution of rotational sub-transitions, forming a band centred around a characteristic Raman shift. Our system's interference filters are to broad to resolve these individual rotational components, so the detected signal integrates over the entire rotational structure, limiting the retrieval to vibrational-level information.

These frequency shifts (Raman shifts) are independent of the laser frequency, and depend only on the molecule's intrinsic properties. Therefore, each species has a different energy shift $\Delta\nu$. In atmospheric applications, nitrogen's (N_2) Raman signal is typically used due to its abundance.

Raman shifts are often expressed in wavenumbers:

$$\Delta\tilde{\nu} = \frac{1}{\lambda_0} - \frac{1}{\lambda_1} \tag{6}$$

where λ_0 is the laser wavelength and λ_1 is the scattered wavelength. For N_2, $\Delta\tilde{\nu} = 2330.7$ cm^{-1} [9, 10].

However, Raman scattering cross-sections are typically 3-4 orders of magnitude lower than elastic ones, meaning only a tiny fraction of photons are inelastically scattered. This significantly limits signal strength and sensitivity.

2.3   Barcelona Raman Lidar

The BRL [1] has been developed to provide high-precision atmospheric calibration for the Cherenkov Telescope Array Observatory (CTAO), an observatory designed to detect very high-energy (VHE) gamma rays via the Cherenkov light emitted by particle showers in the atmosphere. Since atmospheric conditions significantly affect the detection of this light, it is crucial to accurately and continuously measure the vertical distribution of aerosols and molecules along the telescopes' line of sight.

Unlike basic elastic Lidar systems, which measure only the elastically backscattered light, the BRL is capable of also detecting Raman scattering from N_2, allowing for a more precise and selective characterization of the atmosphere. Although Raman scattering is typically several orders of magnitude less frequent than elastic scattering, its spectral shift allows it to be clearly distinguished from the elastic signal. This separation enables a more accurate characterization of the atmosphere, particularly by disentangling contributions from Rayleigh and Mie scattering. Consequently, the detection of both Rayleigh and Raman components improves the retrieval of atmospheric extinction with an accuracy better than 5% [11, 1].

As introduced in Section 2.1, retrieving the extinction profile from elastic Lidar signals (Eq. (1)) requires assuming a value for the LR, which can introduce significant systematic uncertainties due to its variability. The use of a Raman Lidar provides an independent signal at a shifted wavelength, allowing the use of a

modified Lidar equation, given by:

$$P_R(r, \lambda_R) = P_0 \frac{Act_0}{2r^2} \underbrace{\sigma_R(\lambda_E, \lambda_R) n(r)}_{\beta(r, \lambda_E, \lambda_R)} \exp\left\{ - \underbrace{\int_0^r (\alpha(\lambda_E, r') + \alpha(\lambda_R, r')) dr'}_{\tau(r, \lambda_E, \lambda_R)} \right\} \quad (7)$$

Here, λ_E is the emitted (elastic) wavelength, λ_R is the Raman-shifted wavelength, $n(r)$ is the number density of the Nitrogen molecule and $\sigma_R(\lambda_E, \lambda_R)$ represents the differential Raman backscattering cross-section [10].

Since this equation depends only on extinction terms, it allows a direct retrieval of $\tau(r, \lambda_E, \lambda_R)$ without the need to assume a LR. Instead, $\beta(r, \lambda_E, \lambda_R)$ can be subsequently derived from the elastic signal.

By independently measuring the extinction profile through the Raman channel, the backscatter coefficient can be subsequently derived from the elastic channel. This significantly reduces systematic errors, which in purely elastic systems has been shown to reach up to 20% when estimating extinction [5].

2.3.1   Operation

The BRL emits short laser pulses into the atmosphere using a Q-switched Nd:YAG laser [12]. Second (532 nm) and third (355 nm) harmonics of the fundamental 1064 nm line are generated via compact modules containing non-linear crystals and removable dichroic mirrors integrated into the main body of the laser. The resulting beam is guided coaxially using two $5''$ dichroic mirrors, which also suppress residual 1064 nm light not filtered at the laser head [13].

Backscattered light from atmospheric molecules and aerosols is collected by a 1.8-m Newtonian telescope aligned with the laser beam. This alignment ensures efficient photon capture at the focal plane, maximizing the signal collection. Due to its low cross-section, Raman scattering is much weaker than elastic scattering, requiring sensitive detectors and longer integration times.

At the telescope focus, an 8-mm diameter Liquid Light Guide (LLG) transmits the collected light to the polychromator, located in the rear section of the system. The polychromator spectrally resolves the incoming signal using a combination of dichroic mirrors, beam splitters and optical filters to separate the backscattered light into four spectral channels: two elastic (355 nm and 532 nm) and two Raman-shifted wavelengths (387 nm and 607 nm)[2]. Each channel is directed to a photomultiplier tube (PMT), which converts the photon flux into electrical signals.

PMT signals are digitized by a data acquisition system as a function of time. Since light propagates at a known speed, the time delay between emission and detection corresponds to a specific altitude, allowing reconstruction of vertical profiles of molecular and aerosol scattering.

Each laser shot provides a profile of atmospheric extinction at different heights (Eq. (7)). These profiles are the experimental input for retrieving the backscatter coefficient $\beta(r, \lambda)$ and optical depth $\tau(r, \lambda)$, essential for the precise calibration of the CTAO. Typically, several thousand shots are averaged to improve the signal-to-noise ratio.

Fig. 2.1 sketches the prototype version of the Barcelona Raman Lidar (pBRL). Although the current system includes some modifications, detailed in the Section 2.4, the overall layout and functional structure remain essentially unchanged.

---

[2]Using Eq. (6) and the Raman wavenumber of N_2 [9], the Raman shifts correspond to $\Delta\lambda(355$ nm$) = 32$ nm and $\Delta\lambda(532$ nm$) = 75$ nm.
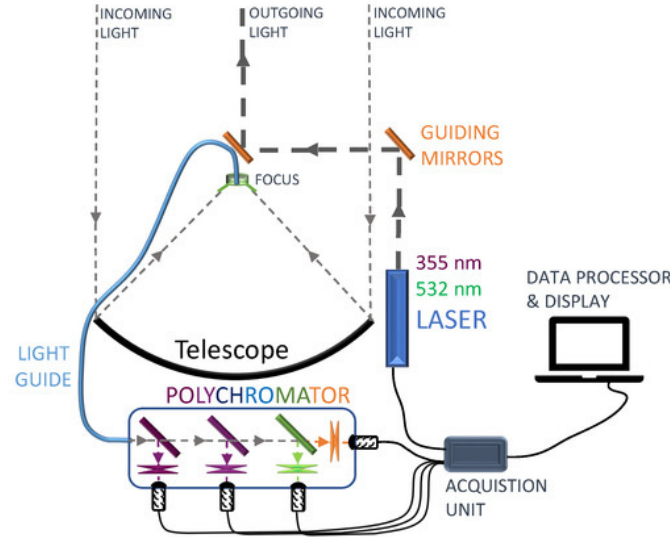
Figure 2.1: Schematic representation of the pBRL system and its main components: the receiver, including the telescope, the polychromator and data acquisition unit, and the transmitter, composed of the laser and guiding mirrors. Figure from [1].

2.4   Characterization

To obtain the required precision for atmospheric calibration, each component of the Lidar system must be carefully characterized. The pBRL has already been successfully tested, demonstrating the viability of the design and its capability to retrieve atmospheric profiles with Raman channels [14]. The final version of the BRL incorporates several important upgrades to improve its performance: a new diode-pumped laser source with higher repetition rate and improved stability, and new gated PMTs for better detection sensitivity.

This work is focused specifically on verifying the performance and stability of the laser emission, as well as the optical quality and focusing properties of the receiving telescope.

2.4.1   Laser

A key part of characterizing the Lidar system involves studying the laser beam's spatial profile and divergence. Although photon emission in a laser is fundamentally a quantum process, in regimes with high photon flux, as is typical in intense laser beams, the spatial distribution of power can be modelled using Gaussian modes. In particular, the irradiance $I(x, y)$, defined as the power per unit area on a transverse plane, can be modelled using the fundamental Gaussian mode as:

$$I(x, y) = I_0 \left(\frac{w_0}{w(z)} \right)^2 \exp\left\{ -2\frac{x^2 + y^2}{w^2(z)} \right\} \tag{8}$$

At a given distance, z can be considered fixed. The parameter $w(z)$ represents the beam radius at position z, defined as the distance from the beam centre at which the irradiance drops to $1/e^2$ of its peak value I_0. The parameter w_0 is the beam waist, the beam radius at the point of its focus ($z = 0$).

Although the fundamental mode transverse electromagnetic mode (TEM_{00}) often dominates in well-behaved lasers, real beams frequently include contributions from higher-order modes and exhibit deviations from perfect radial symmetry. These effects can be profiled using an elliptical Gaussian, introducing different beam widths w_x and w_y along the transverse axes. The irradiance then becomes [15, 16]:

$$I_{mn}(x, y) = I_0 \frac{w_{0,x}}{w_x(z)} \frac{w_{0,y}}{w_y(z)} H_m^2 \left(\frac{\sqrt{2}x}{w_x} \right) H_n^2 \left(\frac{\sqrt{2}y}{w_y} \right) \exp\left\{ -2 \left(\frac{x^2}{w_x^2} + \frac{y^2}{w_y^2} \right) \right\} \tag{9}$$

where H_m and H_n are Hermite polynomials of order m and n.

These deviations can also be quantified by the beam quality factor M^2. This parameter compares the actual beam divergence with that of an ideal Gaussian beam, and is defined through the relation:

$$\theta_{\text{real}} = M^2 \frac{\lambda}{\pi w_0} \tag{10}$$

A perfect Gaussian beam corresponds to $M^2 = 1$, while higher values reflect increasing divergence due to higher-order modes or optical imperfections. The theoretical M^2 of a beam composed of Hermite-Gaussian modes can be calculated from their power contributions:

$$M^2 = \sum_{m,n} P_{mn}(2m+1)(2n+1) \tag{11}$$

where P_{mn} represents the relative power in each mode to the total beam intensity.

In experimental conditions, the divergence can also be estimated directly from the beam width measured at a known distance z from the laser source. For small values of θ, which is typically the case in collimated laser beams:

$$\theta \approx \tan\theta = \frac{2w}{z} \tag{12}$$

The laser datasheet indicates a beam divergence below 2 mrad, but does not provide a specific value for M^2. A similar model reports $M^2 < 2$, which may serve as a rough reference, although it cannot be directly assumed for the current device.

2.4.2 Mirror

In Raman Lidars, inelastic scattering signals (Raman lines) are very weak, due to the small interaction cross-section. To compensate for this, it is crucial to employ a mirror with a large collecting area and excellent optical quality. For this reason, the BRL uses a 1.8-m parabolic primary mirror, providing a large effective collection area that enhances the system's sensitivity to Raman signals.

However, any imperfection in the mirror's surface can introduce optical aberrations that degrade the system performance. Characterizing the mirror's optical behaviour is therefore essential to ensure high efficiency and resolution in detecting the weak Raman signals.

One way of characterizing the mirror is through the analysis of its Point Spread Function (PSF). It describes how a point source of light is imaged by the optical system, representing the spatial distribution of irradiance resulting from that point source.

Ideally, a point source at infinity would be imaged as a perfect point on the focal plane. However, in practice, even a perfect mirror produces a finite-sized image due to diffraction. A real optical system also suffers from aberrations, systematic deviations from the ideal imaging behaviour, which further spread the light beyond the diffraction limit. As a result, the PSF captures not only the unavoidable effects of diffraction but also the imperfections introduced by optical aberrations.

An important property of reflectors is that they do not suffer chromatic aberration, since reflection is almost independent of wavelength, so only monochromatic aberration needs to be considered.

Under the paraxial approximation, light rays are assumed to travel very close to the optical axis, such that $\sin\theta \approx \theta$. This approximation fails for rays farther off-axis. To address this, the sine function can be expanded in a Taylor series including higher-order terms. Considering terms up to third order leads to Seidel's third-order theory, which describes how rays deviating from paraxial behaviour produce imperfections in focusing. These deviations result in the five primary monochromatic aberrations, known as Seidel aberrations [17]:

1. **Spherical Aberration**
   Spherical aberration appears when rays striking the mirror at different distances from the optical axis are not brought to the same focus. While paraxial rays converge at the designed focal point, marginal rays intersect the optical axis at different locations.
   In a Newtonian reflector, the use of a parabolic mirror ideally eliminates spherical aberration. However, slight deviations from the perfect paraboloid shape or mirror deformations can reintroduce residual spherical aberration.

2. **Coma**

   Coma shows up when a point source is not observed in the centre of the field of view. Instead of forming a round spot, the image looks stretched out, like a comet. This aberration arises because rays entering different parts of the aperture do not converge at one point.

3. **Astigmatism**

   Astigmatism causes rays in different tangential planes to focus at different distances from the mirror. Consequently, an image of a point source becomes stretched into a line in one direction. This aberration can become a problem if parts of the optical system are slightly misaligned.

4. **Field curvature**

   Field curvature occurs when the wavefront at the focal distance is curved. As a consequence, while the centre of the image may be in focus, the edges appear blurry if the detector plane is flat. However, in the case of the BRL, this effect is negligible because the detection system is a light collector at the centre of the focal plane.

5. **Distortion**

   Distortion affects the geometry of the image. It causes the magnification to vary across the field, leading to images that are stretched or compressed toward the edges. Like field curvature, it is only relevant when forming a full image on a flat detector plane, so this aberration is not a concern in the current configuration.

3   Laser beam analysis

To characterize the beam profile of a new laser used for the BRL system, a series of experimental measurements and image analyses were carried out. The goals were to determine the beam waist and divergence, to identify the contributing transverse electromagnetic (TEM) modes and to estimate the beam quality factor M^2.

3.1   Experimental setup

The laser was directed towards a graph paper sheet, positioned at a known distance ($z = 68 \pm 1$ m). Images of the laser spot were taken using a digital camera. To preserve raw intensity information for each colour channel, the camera's CR3 RAW files were converted into FITS format, both retaining the full dynamic range of each individual pixel and allowing precise analysis of the full image, including pixel saturation.

All RAW images were examined using the software *RawTherapee*, which allowed us to visually inspect and discard those that were out of focus, overexposed or misaligned. Only clean, well-resolved and unsaturated images were selected. Additionally, the pixel-to-millimetre conversion factor was determined in this software, using the graph paper as a spatial reference to convert pixel measurements into physical dimensions.

3.2   Camera characteristics

The camera used for the acquisition of the experimental images was a Canon EOS R100 [18], equipped with an APS-C CMOS sensor. CMOS sensors in this type of camera consist of a rectangular array of photosensitive pixels, each of which measures the intensity of the incoming light. However, the pixels themselves are not colour-sensitive. To capture colour information, a colour filter array is placed over the sensor, typically following the Bayer pattern [19]. This filter pattern includes two green filters, one red and one blue, giving higher weight to the green channel to match the human eye's greater sensitivity to green light.

Since each pixel captures only one component of the colour information, the full RGB values for each pixel are reconstructed using a process known as demosaicking. This interpolation process estimates the missing colour components based on the values of neighbouring pixels. Each channel also has a different spectral response, determining its sensitivity to light at different wavelengths [20].

Fig. 3.1 shows the RGB transmission curves of a typical Canon APS-C Bayer filter, based on data from a similar model (Canon T3i). Since Canon does not publish the exact spectral characteristics of each sensor model, this approximation is used to illustrate the qualitative behaviour of the RGB channels. The transmission profiles are especially relevant for interpreting the response of each channel to specific wavelengths present in the laser and background.
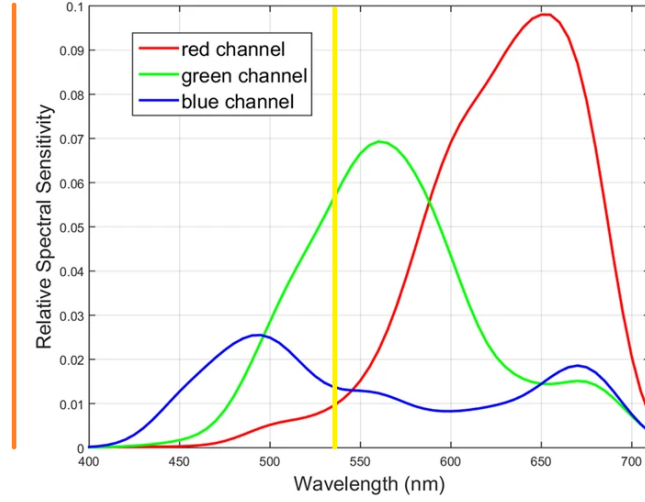
Figure 3.1: Spectral response curves of a Canon T3i APS-C CMOS image sensor equipped with a Bayer pattern colour filter array. The yellow and orange lines indicate approximately the laser wavelengths of 532 nm and 355 nm, respectively. Figure adapted from [21].

3.3   Image analysis

The images were analysed using a custom Python script (see Appendix C). The red channel of the FITS image was used for extracting the laser beam's intensity distribution, as it was the only channel that did not suffer from saturation, ensuring reliable quantitative analysis.

For spatial calibration, the blue channel was used instead. It provided sufficient contrast to accurately identify the paper grid, allowing for precise pixel-to-millimetre conversion, as shown in Fig. 3.2(*left*). This is because the blue filter has a transmission peak near the wavelength range reflected by the graph paper (see Fig. 3.1), making the millimetre lines clearly visible.

After extracting the 2D intensity distribution of the laser beam, the background was subtracted and the image was normalized. The resulting profile is shown in Fig. 3.2(*right*).
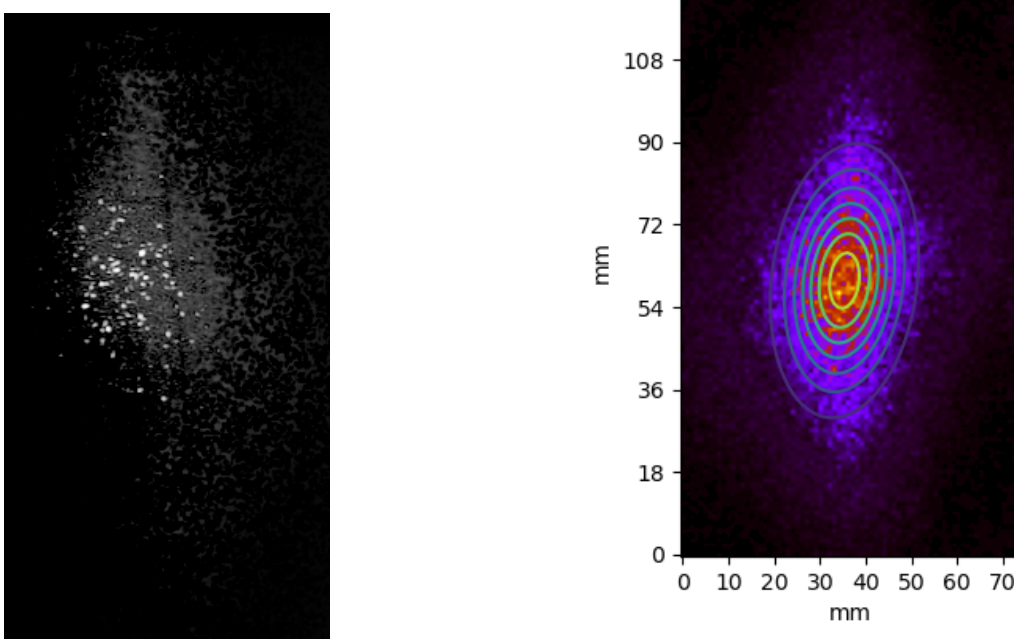

Figure 3.2: *Left:* Blue channel image showing the millimetre grid used for spatial calibration. *Right:* Spatial intensity distribution of the laser beam extracted from the red channel, with ellipsoidal contours fitted to the image.

Fig. 3.3(*left*) shows the encircled energy as a function of radial distance from the beam centre, computed along the major axis (green) and minor axis (red) of an ellipsoid fitted to the image (Fig. 3.2). Each point represents the cumulative fraction of the total intensity enclosed within an expanding ellipse centred on the peak. Ideally, this should approach 1 as all energy is enclosed, indicating that all the beam energy is accounted for. In early versions, the curve slightly exceeded unity in the minor axis due to an improper definition of the background level. Since the intensity was normalized to the maximum pixel value, any residual background noise or slight overestimation in peripheral regions can lead to cumulative intensity above unity. After refining the background subtraction criteria, this overestimation was resolved, and, although it still very slightly exceeds unity, the deviation is negligible. We also see that the intensity is more concentrated along the minor axis, reaching 50% of the total intensity at a smaller radius ($r_{50\%} = 1.3$ cm) compared to the major axis ($r_{50\%} = 2.5$ cm). This confirms the elliptical shape of the beam, with the minor axis approaching the effective beam waist.

To complement this analysis and better estimate the beam waist $w(z)$, I proposed plotting the irradiance profile, shown in Fig. 3.3(*right*). This plot represents the normalized average intensity as a function of radial distance from the beam centre, again for both axes. The rapid decay of intensity in the red curve (minor axis) highlights that the beam is better focused in this direction. The dashed horizontal blue line marks the $1/e^2$ threshold, used to define the beam radius. The intersection of the irradiance curves with this threshold allows for a direct estimation of the beam waist in each direction: 2.21 cm for the minor axis and 4.20 cm for the major axis. The uncertainty of these values is estimated to be ± 0.1 cm, based on the variability observed when modifying the background threshold and fitting parameters during the analysis.
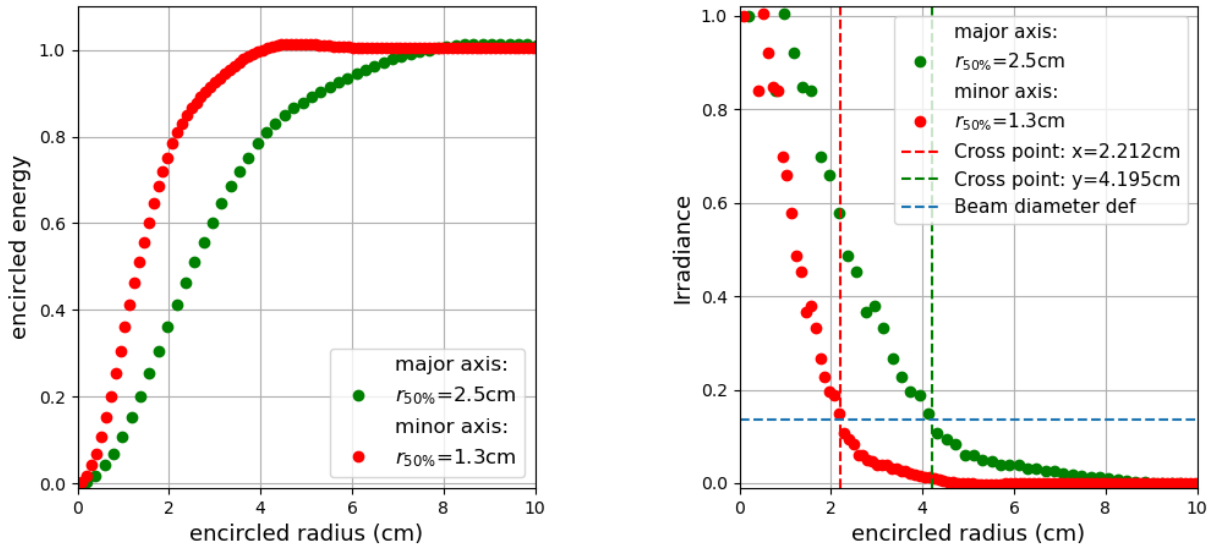

Figure 3.3: Encircled energy (*left*) and normalized irradiance profiles (*right*) along the beam's major and minor axes. The irradiance profiles include vertical dashed lines marking the beam diameter defined by the $1/e^2$ level (horizontal blue dashed line).

Using these beam waist values and the divergence formula in Eq. (12), we obtain the angular divergences along each axis:

$$\theta_x = 0.632 \pm 0.034 \text{ mrad} \qquad\qquad \theta_y = 1.198 \pm 0.045 \text{ mrad} \qquad (13)$$

Both values are well-below the 2 mrad threshold specified in the manufacturer's datasheet, indicating the laser operates within expected performance limits.

3.4   Gaussian beam model

To model the observed laser beam, we fitted the experimental 2D intensity profile using a superposition of Hermite-Gaussian modes. We tested two distinct approaches: a circular model, which assumes a

symmetric beam waist, and an elliptical model, which allows for different beam waists along the two transverse axes. Both models share the same formalism, differing only in the beam parameters used in the Hermite polynomial expressions.

The general form of the intensity model is:

$$I_{\text{model}} = c \sum_{m,n} A_{mn} I_{mn}(x, y, w_x, w_y) \tag{14}$$

where $I_{mn}(x, y, w)$ are the normalized intensity profiles of the modes (Eq. (9)), A_{mn} are their corresponding mode amplitudes, and c is a parameter that accounts both for the global conversion from physical intensity to digital counts recorded by the camera, and for the factor $(w_0/w)^2$. The indices m, n run from 0 to a maximum value to be determined in the analysis. The amplitude of the fundamental mode is fixed to $A_{00} = 1$.

The optimal values of the parameters A_{mn}, c, w_x and w_y were obtained by maximizing the likelihood function based on the residuals between the experimental image and the model:

$$\mathcal{L} = \prod_i \frac{1}{\sqrt{2\pi\sigma^2}} \exp\left\{-\frac{(I_i - I_{\text{model}}(x_i, y_i))^2}{2\sigma^2}\right\} \tag{15}$$

This is equivalent to minimizing the negative log-likelihood.

Before arriving at the final model, we tested several preliminary fits using different combinations of Hermite-Gaussian modes. The goal of this process was to determine which modes contributed meaningfully to the description of the beam profile. Each model was evaluated by analysing the amplitudes of the fitted modes, verifying whether they were significantly different from zero. In addition, the covariance matrix of the fit parameters was examined to identify strong correlations between modes, which could indicate redundancy or overfitting. The visual comparison between the fitted model and the experimental image was also considered as a qualitative measure of how well the model captured the beam shape.

Through this iterative process, modes with negligible amplitude or that were highly correlated with others were systematically discarded. Such modes do not improve the fit in a meaningful way and may introduce numerical instabilities. Additionally, the evolution of the negative log-likelihood function was monitored when including or excluding specific modes in order to quantify whether their presence improved the overall fit. Modes that did not produce a significant increase in the likelihood were excluded. The final selection included only those modes that provided a robust and physically consistent description of the measured intensity distribution, interpreted as the relevant modes composing the laser beam.

To validate the robustness of the results, the minimization of the negative log-likelihood procedure was repeated using different optimization methods (Nelder-Mead, Powell, L-BFGS-B, etc.)[3] and with various initial guesses for the parameters. The final fitted values remained stable across these tests, confirming the reliability of the fitting procedure.

3.4.1   Circular Gaussian beam

We begin by analysing the beam profile under the assumption of circular symmetry, where the beam waist is identical along both transverse directions ($w_x = w_y = w$). Under this constraint, the best performance was achieved using the following combination of Hermite-Gaussian modes:

$$I_{\text{model}} = c\left(I_{00} + A_{01}I_{01} + A_{02}I_{02} + A_{03}I_{03} + A_{04}I_{04}\right) \tag{16}$$

Other modes, such as I_{10}, I_{11}, I_{20} and I_{22} were tested, but their fitted amplitudes were negligible and therefore excluded.

The fitted beam radius is:

$$w = 2.361 \pm 0.010 \text{ cm} \tag{17}$$

---

[3]See Scipy.optimize.minimize

Since the amplitudes are relative to the fundamental mode I_{00}, the percentage contribution of each mode to the total intensity was computed. Table 1 lists the fitted amplitudes and corresponding intensity contributions. The full covariance matrix and the fitted value of c are given in Appendix B.1.

Table 1: Fitted amplitudes A_{mn} and their corresponding percentage contributions P_{mn} to the total beam intensity of each Hermite-Gaussian mode for the circular Gaussian model.

Mode	00	01	02	03	04
$\boldsymbol{A_{mn}}$ (%)	100 (fixed)	16.1 ± 4.7	4.66 ± 0.33	0.75 ± 0.12	0.13 ± 0.50
Percentage (%)	82.3 ± 3.2	13.2 ± 3.9	3.83 ± 0.31	0.62 ± 0.10	0.11 ± 0.42

The results indicate that the beam is predominantly described by the fundamental mode I_{00}, which accounts for more than 80% of the total intensity. The first-order vertical mode I_{01} contributes significantly, followed by smaller contributions from higher-order vertical modes in the vertical direction. We can observe that the fitted amplitude and percentage contribution of the I_{04} mode are compatible with zero within uncertainties. This confirms that higher-order contributions beyond the fourth order do not play a significant role and can be neglected in the beam description safely.

To assess the beam quality, the factor M^2 was estimated in two different ways. First, it was computed from the mode composition of the beam, using Eq. (11).

$$M^2 = 1.46 \pm 0.13 \tag{18}$$

Second, M^2 was estimated from the experimental beam divergence, using Eq. (10). Since the fitted mode composition shows no contribution along the horizontal axis, the beam can be considered nearly ideal in that direction. Therefore, the ratio between vertical and horizontal divergences can be used as an estimate:

$$M^2 = \frac{\theta_y}{\theta_x} = 1.90 \pm 0.12 \tag{19}$$

These two values are incompatible within uncertainties, suggesting that the circular model may not fully capture the beam's characteristics. In particular, the difference in divergence between the two axes indicates that the beam may have an elliptical profile. This motivates the use of a model with different waists along each axis.

3.4.2 Elliptical Gaussian beam

We now consider different beam waists along the horizontal and vertical axes ($w_x \neq w_y$). The best fit was achieved using the following model:

$$I_{\text{model}} = c \left(I_{00} + A_{01}I_{01} + A_{02}I_{02} + A_{03}I_{03} + A_{04}I_{04} + A_{10}I_{10} + A_{20}I_{20} \right) \tag{20}$$

Modes such as I_{11}, I_{22} or higher-order components were tested but found to be negligible, and therefore excluded from the final model.

The fitted beam waists are:

$$w_x = 1.937 \pm 0.077 \text{ cm} \qquad\qquad w_y = 3.302 \pm 0.053 \text{ cm} \tag{21}$$

These values are clearly incompatible within uncertainties, differing by approximately 70%, which confirms the elliptical nature of the beam.

Table 2 shows the fitted amplitudes and intensity contributions of each mode. The covariance matrix and c value are given in Appendix B.2

Table 2: Fitted amplitudes A_{mn} and their corresponding percentage contributions P_{mn} to the total beam intensity of each Hermite-Gaussian mode for the elliptical Gaussian model.

Mode	00	01	02	03	04	10	20
$\boldsymbol{A_{mn}}$ (%)	100 (fixed)	4.7 ± 3.6	2.58 ± 0.36	0.49 ± 0.11	0.12 ± 0.42	3.9 ± 2.3	0.86 ± 0.11
$\boldsymbol{P_{mn}}$ (%)	88.8 ± 3.4	4.2 ± 3.2	2.29 ± 0.33	0.436 ± 0.098	0.11 ± 0.37	3.4 ± 2.0	0.77 ± 0.10

These results show that the beam is still dominated by the fundamental mode I_{00}, with non-negligible contributions from both vertical and now horizontal higher-order modes. The contribution of mode I_{04} is compatible with zero and the mode I_{20} remains small, indicating that truncating the expansion at this order remains a valid approximation.

To evaluate the beam quality in the elliptical case, we used the same method as before: estimating the M^2 factor from the mode composition using Eq. (11). However, in this case we cannot rely on the divergence method, as neither axis can be considered close to an ideal Gaussian beam. The resulting value is:

$$M^2 = 1.42 \pm 0.17 \tag{22}$$

This estimate is compatible within uncertainties with the value obtained from the circular model. Nevertheless, it is slightly smaller, which could indicate that the elliptical model provides a more accurate and ideal description of the beam structure.

3.5   Comparison and discussion

In all cases, the fundamental mode dominates, with minor contributions from higher-order modes. The estimated M^2 values remain below 2, a reference taken from similar laser specifications. Although this reference is not particularly rigorous, values close to 1 support that the beam approximates a fundamental Gaussian profile, despite the presence of higher-order mode contributions.

To evaluate which model best describes the experimental data, we compared the divergences obtained from the fitted irradiance profiles with the experimental ones. Irradiance profiles for each model are shown in Fig. 3.4.
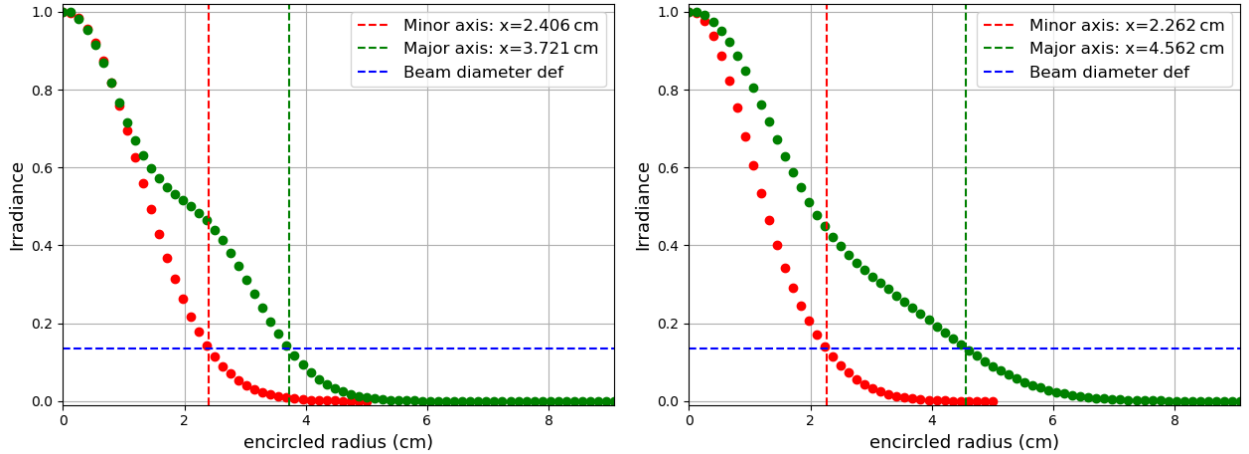

Figure 3.4: Normalized irradiance profiles along the beam's axes for the circular (*left*) and elliptical (*right*) beam models. Vertical dashed lines mark the beam radius where the irradiance drops to $1/e^2$ of the peak value, defining the beam diameter (blue dashed line).

The divergences derived from the intersection points with the $1/e^2$ threshold are:

$$\text{Circular:} \qquad \theta_x = 0.708 \pm 0.031 \text{ mrad} \qquad \theta_y = 1.094 \pm 0.034 \text{ mrad} \tag{23}$$
$$\text{Elliptical:} \qquad \theta_x = 0.665 \pm 0.031 \text{ mrad} \qquad \theta_y = 1.342 \pm 0.035 \text{ mrad} \tag{24}$$

The compatibility with the experimental divergences, using the combined standard deviation is 1.3σ and 0.3σ in the x-axis for the circular and elliptical models, respectively, and 2.9σ and 2.2σ in the y-axis. This supports the conclusion that the elliptical model offers a more realistic description of the beam.

We also compared the spatial irradiance distributions of each model with the experimental profile, shown in Fig. 3.5.
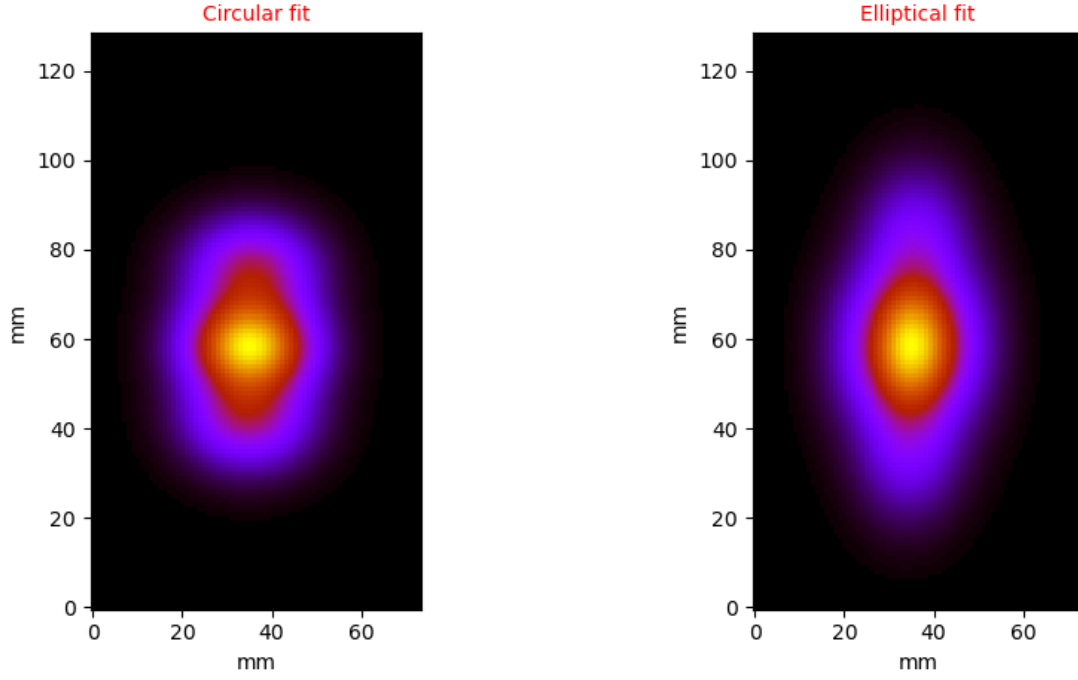
Figure 3.5: Spatial intensity distribution of the circular (*left*) and elliptical (*right*) beam model.

As expected, the elliptical model resembles more closely the experimental irradiance pattern, shown in Fig. 3.2(*right*).

Finally, we computed the reduced chi-squared for both models, yielding $\chi^2/\text{ndf} = 2.31$ for the circular fit and 2.02 for the elliptical one. Although neither model perfectly reproduces the data, the elliptical model shows improved agreement, reinforcing its validity. However, further refinement may still be necessary.

All these comparisons confirm that the elliptical model provides a more accurate and physically consistent representation of the beam. This ellipticity may arise due to asymmetries inside the laser. In diode-pumped lasers, the active region is often non-circular, producing an elliptical TEM_{00} mode. It may also stem from optical components like the dichroic mirror or the beam splitter non-linear crystal. Identifying the exact cause would require further investigation beyond the scope of this work.

4 PSF analysis

4.1 Experimental setup with the initial BRL

As previously discussed, the PSF offers a practical way to evaluate the optical quality of the mirror. To estimate it experimentally, a series of direct observations were performed using celestial sources.

A bright celestial object was selected as a reference, such as Jupiter or Venus, whose real-time coordinates were obtained using the software *Stellarium*. The BRL telescope was manually pointed toward the selected object, and its alignment was finely adjusted until light from the source reached the focal plane, where graph paper was placed to visualize the resulting spot. Photographs of the resulting light distribution were taken using the same digital camera as in Section 3.

4.1.1 PSF results and observations

Initially, Jupiter was chosen to evaluate the PSF of the mirror due to its high brightness and relatively small angular size, which makes it suitable for alignment and focus testing.

It was evident by direct visual inspection that the system was not correctly focused. A manual focusing procedure was therefore carried out: the BRL was pointed toward Jupiter and the position of the focal plane was adjusted by moving the millimetre paper along the optical axis to find the spot with the smallest apparent size. From this, we concluded that the actual focal point lies closer to the mirror than the current detector position. This process was done manually and visually, and thus lacked quantitative precision, but provided useful qualitative insight.

Even at best focus, the observed spot was still highly irregular and extended, showing significant optical aberrations, with astigmatism being particularly evident. We consider several hypotheses to explain the distortion:

- The possibility that the extensions corresponded to Jupiter's moons was explored. However, the positions and brightness of these satellites did not match the observed features. Even the brightest moons would not appear so extended or clearly visible in this setup.

- A misaligned optical axis was considered. To test this, measurements were taken at different telescope pointing angles. The focal plane position remained consistent across different angles, suggesting that the optical axis was not significantly displaced.

- The effect of the zenith angle was discussed. Telescopes generally perform better when pointing near zenith, where gravitational and mechanical deformations are minimized. However, the observed aberrations did not appear to strongly depend on the pointing direction.

- The Moon was also observed. The image appeared highly distorted, confirming the presence of severe optical aberrations.

We attempted to capture an image of Jupiter's spot at the new focus. To quantitatively assess the quality of the PSF, we used the encircled energy method, as in Section 3. We measure the cumulative amount of light contained with concentric circular regions centred on the brightest point of the spot image, and we calculate the radius at which 50%, 80% and 90% of the total energy is enclosed. Smaller values of these parameters indicate a more compact and well-focused PSF, reflecting better optical quality. We performed this analysis for different possible focal positions, and the encircled energy curve corresponding to the best PSF found is shown in Fig. 4.1(*left*).

In a previous study (see [1]), the PSF of the same mirror was characterized. However, their analysis considered only the central region of the spot. Given what we now know about focal distance and astigmatism, a larger area should be considered. Based on these criteria, the 2015 data of [1] were reanalysed, yielding the PSF shown in Fig. 4.1(*right*).
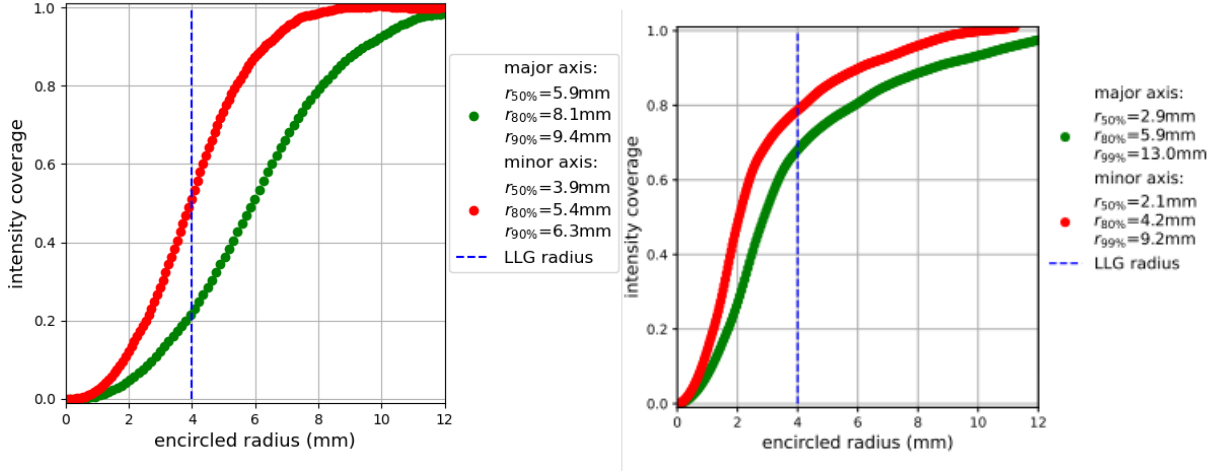
Figure 4.1: Encircled energy curves for the best PSF during Jupiter observation (*left*) and for the reanalysis of PSF data from [1] (*right*), using the same encircled energy criteria. Radii enclosing 50%, 80% and 90% of the total energy are indicated.

The new PSF appears to be approximately 1.5 times broader than the original, indicating a significant degradation in optical quality. Such a change could be a consequence of the successive realuminization and recoating processes the mirror has undergone.

The aluminization process involves depositing a thin layer of aluminium onto the surface of the mirror via vacuum evaporation. This aluminium layer provides high reflectivity, which is essential for efficient light collection in Lidar systems. Following this, a protective coating layer of quartz was applied to protect the reflective layer from oxidation and environmental damage. However, these procedures can potentially alter the optical surface characteristics, affecting the shape and width of the PSF when compared to the one initially characterized.

At naked eye, the aberrations seem more pronounced near the outer edges of the mirror. The BRL features adjustable petals that can partially obstruct the aperture. Therefore, measurements were also taken with the petals partially closed to block the most aberrated regions of the mirror. This adjustment resulted in a noticeable improvement in the observed PSF, shown in Fig. 4.2.
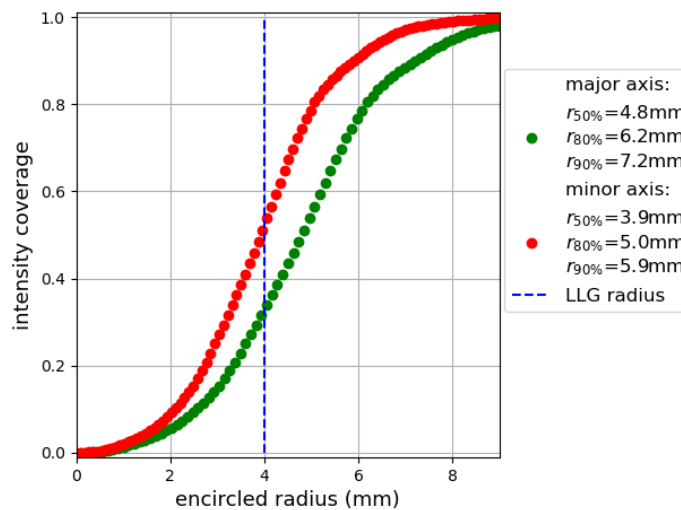

Figure 4.2: Encircled energy curve with petals partially closed.

Nonetheless, comparing with the original PSF shown in Fig. 4.1(*right*), the current optical quality remains significantly degraded.

It is also worth noting that the measurement conditions during our observations were not optimal. Ambient light from nearby street lamps introduced background illumination, reducing contrast and potentially affecting the quality of the captured images.

Besides the chemical treatment, mechanical stress during transport may have also contributed to optical degradation. The mirror was transported twice between the Institut de Física d'Altes Energies (IFAE) and the Observatorio del Roque de los Muchachos (ORM) in La Palma. During this process, it was reported that the transport company accidentally dropped the container in which the BRL was stored. Even if no visible damage occurred, such an impact could have introduced microscopic deformations or misalignments in the mirror substrate or coating, which can degrade the optical performance, introducing additional aberrations and broadening the PSF.

Overall, the current PSF indicates that the mirror has degraded considerably since its initial characterization. Whether the mirror can still be used effectively for precise Lidar measurements under these conditions remains an open question.

4.2   Alternative mirror test and current status

Given the observed degradation of the BRL mirror and the uncertainties regarding its current optical performance, we decided to carry out a test using a spare mirror available. The goal was to evaluate whether this alternative mirror could offer improved optical quality and more reliable PSF measurements.

In order to perform this test, the entire optical assembly had to be reconfigured. This involved adapting the mechanical support structure and transferring the associated electronic components from the original BRL setup to the new configuration. The process was slow due to the mechanical complexity and the need for precise alignment and electrical reconnection.

One trade-off of using the spare container is its reduced field of view compared to the BRL mirror. As a result, the portion of the sky that can be observed is smaller, which could limit the characterization if there is no celestial body sufficiently bright.

Recent measurements attempts have faced additional challenges. There is a strong artificial light source illuminating the mirror during the tests, preventing meaningful measurements due to excessive background light. Moreover, the electronics responsible for moving the mirror towards the zenith are malfunctioning. The system currently only allows azimuthal rotation and produces unusual noises during operation. These technical difficulties have so far prevented a full characterization of the alternative mirror's PSF. Further improvements to the setup are required before conclusive results can be obtained.

5   Conclusions

In this thesis, we have conducted a detailed optical characterization of the main components of the Barcelona Raman Lidar system, focusing on a new laser and the mirror. The goal was to evaluate the current performance of the system and identify limitations that could affect the quality of atmospheric measurements.

We first analysed the laser beam, comparing experimental irradiance measurements with theoretical models. Initially, we applied a circular Hermite-Gaussian mode model, which did not adequately reproduce the observed beam profile. A more refined elliptical Gaussian model provided a significantly better fit to the data, capturing the beam's asymmetry and offering a more realistic description of its propagation. Although we could not determine exactly why the beam is elliptical, we discuss several possible explanations, including asymmetries in the non-linear crystal or the dichroic mirrors inside the harmonic generators. These hypotheses could be explored in more detail in future studies.

The retrieved beam quality factor was $M^2 = 1.42 \pm 0.17$, better than the guaranteed value. However, the best fit model still deviates by 2σ for the major beam diameter and shows a $\chi^2/\mathrm{ndf} = 2$, indicating residual shortcomings of the final model.

We then studied the optical response of the system's Newtonian reflector by experimentally measuring its PSF. During data acquisition, it became clear that the image was out of focus, so we attempted to perform the measurements at what we found to be the true focal plane. These measurements were compared to the expected ideal response and the mirror's original characterization from 2015. The results revealed significant optical aberrations, mainly astigmatism and spherical aberration, which caused strong deformation and elongation of the focal spot. Several hypothesis were proposed to explain this degradation, including damage during transport or bad recoating. The mirror is therefore no longer suitable for use. Consequently, we decided to replace it by a spare mirror. This task remains open for future work.

Our PSF measurements also presented observational challenges. To resolve the focal spot properly, we required a very bright point-like source, clear sky without clouds and minimal ambient light. These strict conditions limited the number of opportunities for successful data collection, further highlighting the practical difficulties of system characterization in real conditions.

Initially, the project also aimed to include a broader analysis of the overall performance of the prototype Barcelona Raman Lidar system and potentially acquire new measurement data using the current system. However, due to the complexity of the tasks, the technical difficulties encountered and the limited time available, these goals could not be fulfilled. They remain as valuable directions for future research.

This work highlights the importance of precise optical modelling and diagnostics in the optimization of Raman Lidar systems. Understanding both the laser beam's real properties and the mirror's optical imperfections is essential for improving signal collection efficiency and enhancing the quality of atmospheric measurements. The results and insights from this project contribute to the ongoing effort to improve the performance and reliability of the BRL system.

References

[1] Otger Ballester, Oscar Blanch, Joan Boix, et al. A 1.8 m class pathfinder raman lidar for the northern site of the cherenkov telescope array observatory—technical design. *Remote Sensing*, 17(6), 2025.

[2] B. S. Acharya, M. Actis, T. Aghajani, et al. Introducing the CTA concept. *Astroparticle Physics*, 43:3–18, 2013. doi: 10.1016/j.astropartphys.2013.01.007.

[3] The Cherenkov Telescope Array Consortium, B. S. Acharya, I. Agudo, et al. *Science with the Cherenkov Telescope Array*. World Scientific, 2019. Edited by the CTA Consortium.

[4] Gary G. Gimmestad and David W. Roberts. *Lidar Engineering: Introduction to Basic Principles*. Cambridge University Press, 2023.

[5] A. López Oramas et al. The ifae/uab and lupm raman lidars for the cta observatory. In *33rd International Cosmic Ray Conference (ICRC2013)*, Rio de Janeiro, Brazil, 2013.

[6] Chiao-Yao She and Jonathan S. Friedman. *Atmospheric Lidar Fundamentals: Laser Light Scattering from Atoms and Linear Molecules*. Cambridge University Press, 2022.

[7] F. R. S. Lord Rayleigh. XXXIV. On the transmission of light through an atmosphere containing small particles in suspension, and on the origin of the blue of the sky. *The London, Edinburgh, and Dublin Philosophical Magazine and Journal of Science*, 47(287):375–384, 1899. `https://doi.org/10.1080/14786449908621276`.

[8] Claudio Tomasi, Vito Vitale, Boyan Petkov, et al. Improved algorithm for calculations of rayleigh-scattering optical depth in standard atmospheres. *Appl. Opt.*, 44(16):3320–3341, Jun 2005. `https://opg.optica.org/ao/abstract.cfm?URI=ao-44-16-3320`.

[9] José Alex Zenteno-Hernández, Adolfo Comerón, Alejandro Rodríguez-Gómez, et al. A Comparative Analysis of Aerosol Optical Coefficients and Their Associated Errors Retrieved from Pure-Rotational and Vibro-Rotational Raman Lidar Signals. *Sensors*, 21(4), 2021. `https://www.mdpi.com/1424-8220/21/4/1277`.

[10] C. Weitkamp. *Lidar: Range-Resolved Optical Remote Sensing of the Atmosphere*, volume 102 of *Springer Series in Optical Sciences*. Springer, 2005.

[11] M. Barceló et al. Development of raman lidars made with former clue telescopes for cta. In *32nd International Cosmic Ray Conference (ICRC2011)*, Beijing, China, 2011.

[12] Nano DPSS-200 Pulsed Q-switched Nd:YAG laser. `https://www.litronlasers.com/product-range/compact-lasers/nano-dpss-range/`, Last accessed: 11/06/2025.

[13] Markus Gaug et al. The ifae/uab raman lidar for the cta-north. *EPJ Web of Conferences*, 197:02005, 2019. AtmoHEAD 2018.

[14] Pedro José Bauzá-Ruiz, Oscar Blanch, Paolo G. Calisse, et al. 1.8 m class pathfinder raman lidar for northern site of cherenkov telescope array observatory—performance. *Remote Sensing*, 17(11), 2025.

[15] Francesco Pampaloni and Joerg Enderlein. Gaussian, hermite-gaussian, and laguerre-gaussian beams: A primer, 2004. `https://arxiv.org/abs/physics/0410021`.

[16] A. E Siegman. *Lasers / Anthony E. Siegman*. University Science Books, Mill Valley, Calif, 1986.

[17] Eugene Hecht. *Optics*. Addison-Wesley, 3rd edition, 1998.

[18] Canon EOS R100 Especificaciones. `https://www.canon.es/cameras/eos-r100/specifications/`, Last accessed: 11/06/2025.

[19] Bryce E. Bayer. Color imaging array, July 1976. `https://patents.google.com/patent/US3971065A/en`.

[20] Xin Li, Bahadir Gunturk, and Lei Zhang. Image demosaicing: a systematic survey. In William A. Pearlman, John W. Woods, and Ligang Lu, editors, *Visual Communications and Image Processing 2008*, volume 6822, page 68221J. International Society for Optics and Photonics, SPIE, 2008. `https://doi.org/10.1117/12.766768`.

[21] Jason Deglint, Farnoud Kazemzadeh, Daniel Cho, et al. Numerical demultiplexing of color image sensor measurements via non-linear random forest modeling. *Scientific Reports*, 6:28665, 2016. `https://doi.org/10.1038/srep28665`.

A   Standard deviation of the Likelihood

The parameter σ in Eq. (15), representing the standard deviation of the noise in the image of the laser, was estimated iteratively. First, a preliminary value of $\sigma \approx 6 \cdot 10^{-5}$ was assumed based on the observed fluctuations. Using this initial estimate, the negative log-likelihood was minimized to obtain a first set of optimal parameters.

With these parameters, the distribution of the residuals $I_i - I_{\mathrm{model}}(x_i, y_i)$ was analysed. Fig. A.1 shows a histogram of the residuals, weighted by the model intensity to reflect their contribution to the likelihood. The distribution is approximately Gaussian and centred around zero.

The weighted standard deviation of the histogramed residuals was taken as a refined estimate of the noise level, yielding $\sigma = 8 \cdot 10^{-5}$. This updated value was used to obtain the final set of fitted parameters with improved accuracy.
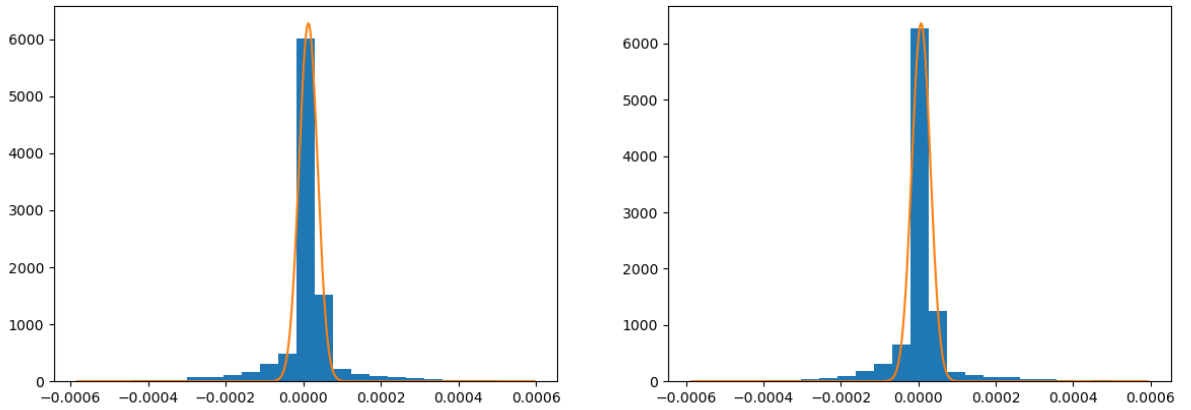

Figure A.1: Histograms of the residuals $I_i - I_{\mathrm{model}}(x_i, y_i)$ for the circular (*left*) and elliptical (*right*) Gaussian models. For the circular model, $\sigma = 8.8 \cdot 10^{-5}$, while for the elliptical model $\sigma = 8.3 \cdot 10^{-5}$.

B   Beam model parameters

This appendix provides the values of the fitted normalization constant c and the covariance matrix of the fitted parameters for each of the beam models considered in the analysis.

B.1   Circular Beam Model

The fitted normalization constant is:

$$c = (1.076 \pm 0.043) \cdot 10^{-3}$$

The covariance matrix for the parameters: $p = \left[w/100, A_{01}, A_{02} \cdot 10, A_{03} \cdot 10^2, A_{04} \cdot 10^2, c \cdot 10^3\right]$ (the extra factors are for a more accurate fit) is:

$$\text{cov}\,(p_0) = \begin{pmatrix} 5.9 \cdot 10^{-7} & -1.2 \cdot 10^{-6} & -2.8 \cdot 10^{-6} & -5.4 \cdot 10^{-6} & 6.5 \cdot 10^{-7} & -1.4 \cdot 10^{-6} \\ -1.2 \cdot 10^{-6} & 2.2 \cdot 10^{-3} & -1.5 \cdot 10^{-3} & 1.2 \cdot 10^{-3} & 2.3 \cdot 10^{-2} & -2.0 \cdot 10^{-3} \\ -2.8 \cdot 10^{-6} & -1.5 \cdot 10^{-3} & 1.1 \cdot 10^{-3} & -7.4 \cdot 10^{-4} & -1.6 \cdot 10^{-2} & 1.3 \cdot 10^{-3} \\ -5.4 \cdot 10^{-6} & 1.2 \cdot 10^{-3} & -7.4 \cdot 10^{-4} & 1.4 \cdot 10^{-2} & 1.2 \cdot 10^{-2} & -1.1 \cdot 10^{-3} \\ 6.5 \cdot 10^{-7} & 2.3 \cdot 10^{-2} & -1.6 \cdot 10^{-2} & 1.2 \cdot 10^{-2} & 2.6 \cdot 10^{-1} & -2.2 \cdot 10^{-2} \\ -1.4 \cdot 10^{-6} & -2.0 \cdot 10^{-3} & 1.3 \cdot 10^{-3} & -1.1 \cdot 10^{-3} & -2.2 \cdot 10^{-2} & 1.9 \cdot 10^{-3} \end{pmatrix}$$

B.2   Elliptical Beam Model

The fitted normalization constant is:

$$c = (1.148 \pm 0.039) \cdot 10^{-3} \tag{25}$$

The covariance matrix for the parameters: $p = \left[w_y/100, A_{01}, A_{02} \cdot 10, A_{03} \cdot 10^2, A_{04} \cdot 10^2, c \cdot 10^3, w_x/100, A_{10}, A_{20}\right]$ is:

$\text{cov}\,(p_0) =$

$$= \begin{pmatrix} 1.6 \cdot 10^{-5} & -3.1 \cdot 10^{-5} & -4.9 \cdot 10^{-5} & -1.3 \cdot 10^{-4} & -4.9 \cdot 10^{-5} & 2.3 \cdot 10^{-5} & 1.3 \cdot 10^{-5} & -5.3 \cdot 10^{-5} & -1.4 \cdot 10^{-6} \\ -3.1 \cdot 10^{-5} & 1.3 \cdot 10^{-3} & -1.0 \cdot 10^{-3} & 7.5 \cdot 10^{-4} & 1.4 \cdot 10^{-2} & -1.4 \cdot 10^{-3} & -3.9 \cdot 10^{-5} & 2.0 \cdot 10^{-4} & 1.4 \cdot 10^{-5} \\ -4.9 \cdot 10^{-5} & -1.0 \cdot 10^{-3} & 1.3 \cdot 10^{-3} & 9.6 \cdot 10^{-5} & -1.3 \cdot 10^{-2} & 1.1 \cdot 10^{-3} & -6.1 \cdot 10^{-5} & 2.0 \cdot 10^{-4} & -2.3 \cdot 10^{-6} \\ -1.3 \cdot 10^{-4} & 7.5 \cdot 10^{-4} & 9.6 \cdot 10^{-5} & 1.2 \cdot 10^{-2} & 6.0 \cdot 10^{-3} & -8.1 \cdot 10^{-4} & -2.1 \cdot 10^{-4} & 8.4 \cdot 10^{-4} & 2.7 \cdot 10^{-5} \\ -4.9 \cdot 10^{-5} & 1.5 \cdot 10^{-2} & -1.3 \cdot 10^{-2} & 6.0 \cdot 10^{-3} & 1.7 \cdot 10^{-1} & -1.6 \cdot 10^{-2} & -1.2 \cdot 10^{-4} & 9.8 \cdot 10^{-4} & 1.3 \cdot 10^{-4} \\ 2.3 \cdot 10^{-5} & -1.4 \cdot 10^{-3} & 1.1 \cdot 10^{-3} & -8.1 \cdot 10^{-4} & -1.6 \cdot 10^{-2} & 1.6 \cdot 10^{-3} & 4.8 \cdot 10^{-5} & -2.4 \cdot 10^{-4} & -1.7 \cdot 10^{-5} \\ 1.3 \cdot 10^{-5} & -3.9 \cdot 10^{-5} & -6.1 \cdot 10^{-5} & -2.1 \cdot 10^{-4} & -1.2 \cdot 10^{-4} & 4.8 \cdot 10^{-5} & 3.4 \cdot 10^{-5} & -1.3 \cdot 10^{-4} & -3.7 \cdot 10^{-6} \\ -5.3 \cdot 10^{-5} & 2.0 \cdot 10^{-4} & 2.0 \cdot 10^{-4} & 8.4 \cdot 10^{-4} & 9.8 \cdot 10^{-4} & -2.4 \cdot 10^{-4} & -1.3 \cdot 10^{-4} & 5.1 \cdot 10^{-4} & 1.3 \cdot 10^{-5} \\ -1.4 \cdot 10^{-6} & 1.4 \cdot 10^{-5} & -2.3 \cdot 10^{-6} & 2.7 \cdot 10^{-5} & 1.3 \cdot 10^{-4} & -1.7 \cdot 10^{-5} & -3.7 \cdot 10^{-6} & 1.3 \cdot 10^{-5} & 1.2 \cdot 10^{-6} \end{pmatrix}$$

C   Python codes

The complete Python code of the laser beam analysis and the fit Circular model is available in:
`analysis_beam_Circular`

The complete Python code of the laser beam analysis and the fit Elliptical model is available in:
`analysis_beam_Elliptic`

The complete Python code of the PSF Analysis of the Newtonian reflector is available in:
`PSF_Analysis`